Acta Materialia 186 (2020) 116–123

Contents lists available at ScienceDirect

Acta Materialia

journal homepage: www.elsevier.com/locate/actamat

Full length article

Pressureless two-step sintering of ultrafine-grained tungsten

Xingyu Li[a], Lin Zhang[a,*], Yanhao Dong[b,**], Rui Gao[b], Mingli Qin[a], Xuanhui Qu[a], Ju Li[b,c,***]

[a] Beijing Advanced Innovation Center for Materials Genome Engineering, Institute for Advanced Materials and Technology, University of Science and Technology Beijing, Beijing 100083, China
[b] Department of Nuclear Science and Engineering, Massachusetts Institute of Technology, Cambridge, MA 02139, USA
[c] Department of Materials Science and Engineering, Massachusetts Institute of Technology, Cambridge, MA 02139, USA

ARTICLE INFO

Article History:
Received 27 November 2019
Revised 24 December 2019
Accepted 1 January 2020
Available online 6 January 2020

Keywords:
Porosity
Two-step sintering
Ultrafine-grained materials
Grain growth
Mechanical properties

ABSTRACT

The challenge of producing dense ultrafine-grained (UFG) tungsten is hereby addressed by a simple pressureless two-step sintering method. It provides a uniform microstructure with ~99% theoretical density and ~700 nm grain size, which is among the best sintering practice of pure tungsten reported in the literature. Benefitting from the finer and more uniform microstructures, two-step sintered samples show better mechanical properties in bending strength and hardness. While parabolic grain growth kinetics is verified, a transition in the nominal grain boundary mobility was observed at 1400 °C, above which the effective activation enthalpy is ~6.1 eV, below which grain boundary motion is rapidly frozen with unusually large activation enthalpy of ~12.9 eV. Such highly nonlinear behavior in activation parameters with respect to temperature suggests that activation entropy and maybe collective behavior play a role in grain growth. We believe the as-reported two-step sintering method should also be applicable to other refractory metals and alloys, and may be generalized to multi-step or continuous-cooling sintering design using machine learning.

1. Introduction

Refractory metals of tungsten (W), molybdenum (Mo), tantalum (Ta), niobium (Nb), rhenium (Re) etc. are a family of materials that have high melting temperature and special properties such as superior high-temperature strength and corrosion resistance to liquid metal [1]. The high melting temperature makes conventional processing routes of liquid metallurgy (e.g., melt casting) followed by cold/hot rolling expensive and difficult. Instead, powder metallurgy and solid-state sintering is the preferred method for consolidation and processing [2]. Nevertheless, sintering such materials to high densities while maintaining fine grain sizes is challenging and typically requires very high temperature (>1700 °C) and controlled atmosphere (e.g., H_2), and often needs to be assisted by mechanical pressure, electric field and/or microwave [3]. The latter are commonly practiced in hot press (HP) [4], hot isostatic press (HIP) [5] and spark plasma sintering (SPS) [6,7], yet these methods offer very limited sample geometry and the cost for processing scales up rapidly with the sample dimension. On the other hand, activated sintering of refractory metals has been known for a long time, where the addition of some low-melting-temperature metals could greatly enhance sintering kinetics and lower the sintering temperature, possibly by changing grain boundary structure/chemistry and/or forming a liquid phase. [8-12] However, such an approach may not be beneficial for subsequent high-temperature applications and is not suitable for many other situations where high purity is a necessity. Furthermore, since ultrafine-grained and nanocrystalline materials are often desirable in terms of improved properties, it would be great to minimize grain growth during sintering. Therefore, decoupling the kinetics of sintering (porosity reduction) and grain growth (grain size increase) and obtaining high-purity, dense, ultrafine-grained refractory metals via pressureless sintering are of great interest [2, 13-18].

Two-step sintering is an effective solution to the above conundrum [19-21]. It modifies the heating schedule of pressureless sintering by (i) firstly heating up the powder compact to a higher temperature T_1 and obtaining 70%–90% theoretical density, (ii) and then cooling down to a lower temperature T_2 to achieve full density with little or no grain growth. It is based on the observation that the nominal grain boundary (GB) mobility (which enables grain growth) can have a much larger activation enthalpy than GB diffusion (which enables porosity reduction and sintering) in certain temperature range, so that a low temperature at T_2 can effectively suppress grain boundary motion (vertical to the GB) while still maintaining active grain boundary diffusion (along GB) for porosity reduction (sintering). Despite the simplicity, it has been

* Corresponding author at: Beijing Advanced Innovation Center for Materials Genome Engineering, Institute for Advanced Materials and Technology, University of Science and Technology Beijing, Beijing 100083, China.
** Corresponding author at: Department of Nuclear Science and Engineering, Massachusetts Institute of Technology, Cambridge, MA 02139, USA.
*** Corresponding author at: Department of Nuclear Science and Engineering & Department of Materials Science and Engineering, Massachusetts Institute of Technology, Cambridge, MA 02139, USA.
E-mail addresses: zlin@ustb.edu.cn (L. Zhang), dongyh@mit.edu (Y. Dong), liju@mit.edu (J. Li).

https://doi.org/10.1016/j.actamat.2020.01.001
1359-6454/

successfully practiced in a variety of ceramics with different chemistries and crystal structures, offering dense fine-grain ceramics with grain size ranging from 50 nm to 1 μm and much improved properties [22-27]. Being a generic method, there is no clear reason why two-step sintering does not work in refractory metals, which motivates us to check its effectiveness in several model metallic systems. Hopefully, our work would not only enable the pressureless sintering of ultrafine-grained/nanocrystalline refractory metals, but also shed light on the intriguing fundamentals of grain growth kinetics.

We start by presenting the pressureless sintering results in pure W, which has the highest melting temperature of 3422 °C among all elemental metals. W has a wide range of important applications in electronic, aerospace, nuclear fusion, and chemical industries. [2] To date, the best practices in the literature provided it a grain size of (i) 800 nm with 95.5% theoretical density (TD) [28] and (ii) 600 nm with 98.1% TD [14], but they used either (i) ultra-high pressure of 2.7 GPa at room temperature or (ii) a "warm" press of 800 MPa at 450 °C to improve the packing of nano W powders in the green body, the pressure conditions of which are not easily obtainable in most laboratories. In the present work, we show through a systematic investigation that W green bodies uniaxially pressed at modest pressure and room temperature can be pressurelessly sintered to 1.6 μm grain size with 98.5% TD by normal sintering (NS), and to 0.7 μm grain size with 98.6% TD by two-step sintering (TSS), the latter of which decreases grain size by a factor of 2 while homogenizing the grain sizes with a much narrower grain size distribution. Measured nominal grain boundary mobility in dense samples identifies activation enthalpy switching from 6.1 eV at high-temperature regime of 1400–1500 °C to an unusually large value of 12.9 eV at low-temperature regime of 1300 °C–1400 °C, analogous to a mobility transition previously seen in yttria-stabilized zirconia [29]. Such a rapidly quenched grain boundary mobility provides a kinetics basis for the two-step sintering in W to achieve ultra-fine grain size. We then show the mechanical properties of two-step sintered W can greatly benefit from the finer and more uniform microstructure, where bending strength, hardness and its Weibull modulus are greatly improved.

2. Experimental procedures

High-purity W powders (purity: 99.9%; particle size: D_{50} = 50 nm) were prepared by solution combustion method previously reported [30]. They were uniaxially pressed into pellets (diameter: 10 mm, thickness: 3 mm) under 750 MPa at room temperature, and subsequently sintered in a flowing hydrogen atmosphere (flow rate: 0.6 L/min). For normal sintering (NS), samples were heated to 1100–1500 °C at 5 °C/min and sintered isothermally. For two-step sintering (TSS), samples were firstly heated to T_1 at 5 °C/min and held for 1 h, then cooled down to T_2 and held for different times. When desired, interrupted runs after the first sintering step or during the second sintering step were also performed to track microstructure evolution before reaching full density. Sample densities were measured by the Archimedes method with a theoretical density of 19.35 g/cm^3 and confirmed with scanning electron microscopy (SEM).

Fractured surfaces of sintered samples were investigated under SEM (FEI Quanta FEG 450), showing intergranular fracture in all cases. Electron backscatter diffraction (EBSD; using diffractometer HKL Channel 5 on Zeiss Ultra 55 field emission scanning electron microscope) was conducted on polished surfaces (prepared by mechanically polishing down to 1 μm followed by Ar ion polishing) to analyze grain structure, grain orientations and misorientation of grain boundaries. Transmission electron microscopy (TEM; FEI Tecnai G2) samples were prepared by focused ion beam (FIB; FEI Helios NanoLab 600i). Average grain sizes were determined from over 100 grains in SEM images of fractured surfaces. Three-point bending strength were measured at room temperature on 1.1 × 1.0 × 12.0 mm^3 samples with a span length of 7 mm under a loading rate of 0.5 mm/min. Nanoindentation measurements (Nano Indenter II, MTS Systems) were conducted at polished surfaces (4 indents for each sample). Continuous stiffness measurements were used up to a max indentation depth of 2000 nm (equivalent to constant strain rate of 0.05 s^{-1} with a Poisson's ratio of 0.25). For nanoindentation measurements, hardness H_{avg} was calculated from its average value at displacements of 1500–1600 nm and reduced Young's modulus E_r was calculated from the unloading curve. Vickers microhardness were tested on polished surfaces under 200 gf (1.96 N) loading and 15 s duration using Vickers diamond pyramid indenter. The distance between different indents was set as 500 μm. Weibull modulus m was calculated from hardness H following the statistics

$$p(H) = 1 - \exp\left[-(H/H_0)^m\right] \quad (1)$$

where H_0 is the characteristic hardness and probability estimator $p(H)$ is calculated by

$$p(H) = (i - 0.3)/(n + 0.4) \quad (2)$$

where i is the rank of the hardness and n = 25 is the total number of hardness measurements. The form of Eq. (2) was chosen to better linearize skewed Weibull data [31].

3. Results

3.1. Sintering kinetics and grain size-density trajectory

Before practicing two-step sintering (TSS), we first investigated the sintering and grain growth behavior of W in normal sintering (NS). Setting a constant holding time for 1 h, the density of samples sintered at 1100–1500 °C increased from 76.2% of theoretical one to 97.2% (shown in Table 1). Further extending holding time to 3 h at 1500 °C and 1600 °C provided a close-to-theoretical density of 98.5% with 1.60 μm grain size and 99.5% with 3.98 μm grain size, respectively. The microstructures of all samples remain relatively uniform with equiaxial grains as shown by fracture surfaces in Fig. 1, yet significant coarsening takes place in NS especially when the density reaches > 90%. Tracked grain size-density trajectory with a concave shape (red dash line in Fig. 2) confirms this trend with accelerating grain growth. This is due to gradual loss of pore pinning, especially during final-stage sintering when pore channels break up into isolated ones above 90%–92% theoretical density, a well-known problem in solid-state sintering.

Two-step sintering was next conducted under various conditions. Full density was successfully reached by first sintering at T_1 from 1300 °C to 1450 °C for 1 h and then at T_2=T_1–100 °C for 10 h. (See data in Table 1) The lowest set of T_1/T_2=1300/1200 °C (sample TSS-1 in Table 1) yields a density of 98.6% with 0.70 μm grain size (Fig. 3a). TEM in Fig. 3b show clean grain boundaries without any second-phase particles or grain-boundary liquid phases. Higher density can be obtained at higher T_1/T_2, at the expense of slightly increased grain size (samples TSS-2, TSS-3, and TSS-4 in Table 1). Microstructures of all the samples (Fig. 3) are uniform without abnormal grains.

Table 1
Density and grain size data for normal sintering and two-step sintering.

	Sintering condition	Density (%)	Grain size (μm)
NS-1	1100 °C for 1 h	76.2	0.30
NS-2	1200 °C for 1 h	79.2	0.37
NS-3	1300 °C for 1 h	88.7	0.53
NS-4	1400 °C for 1 h	93.3	0.86
NS-5	1500 °C for 1 h	97.2	1.24
NS-6	1500 °C for 3 h	98.5	1.60
NS-7	1600 °C for 3 h	99.6	3.98
TSS-1	1300 °C for 1 h, 1200 °C for 10 h	98.0	0.70
TSS-2	1350 °C for 1 h, 1250 °C for 10 h	98.8	0.75
TSS-3	1400 °C for 1 h, 1300 °C for 10 h	98.9	0.87
TSS-4	1450 °C for 1 h, 1350 °C for 10 h	99.1	0.95

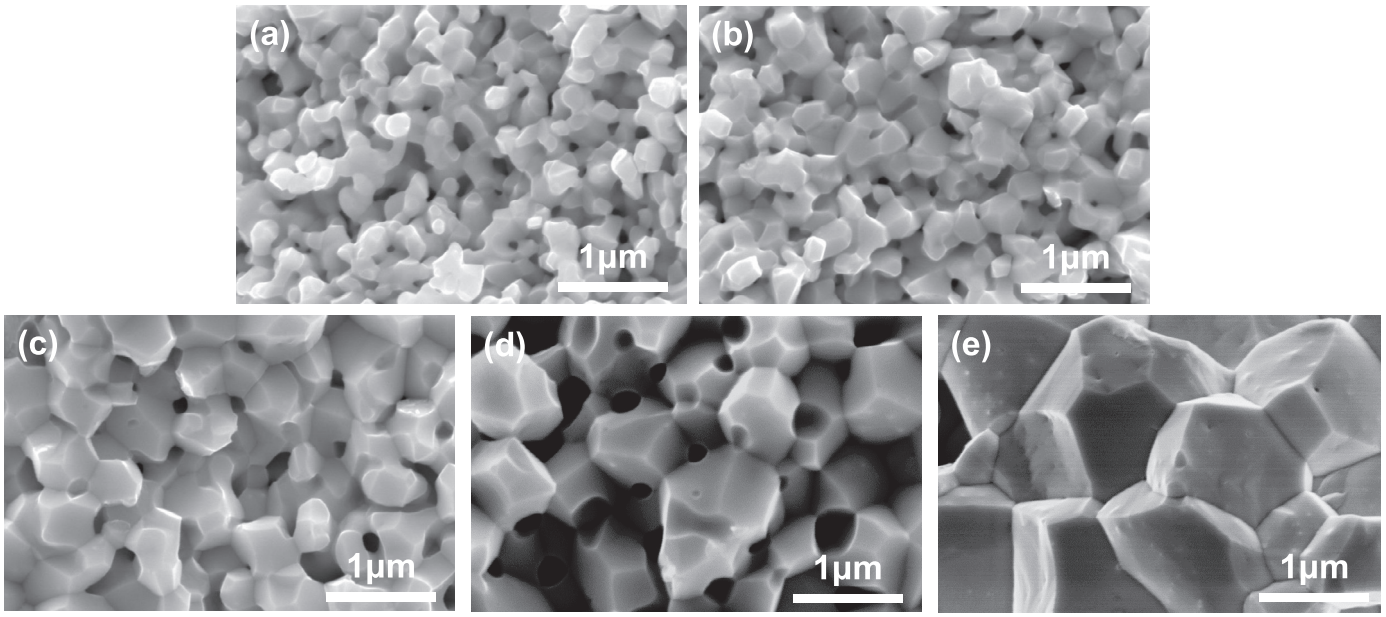

Fig. 1. Fracture surfaces of samples normally sintered at (a) 1100 °C, (b) 1200 °C, (c) 1300 °C, (d) 1400 °C for 1 h, (e) 1500 °C for 3 h and (e) 1600 °C for 3 h.

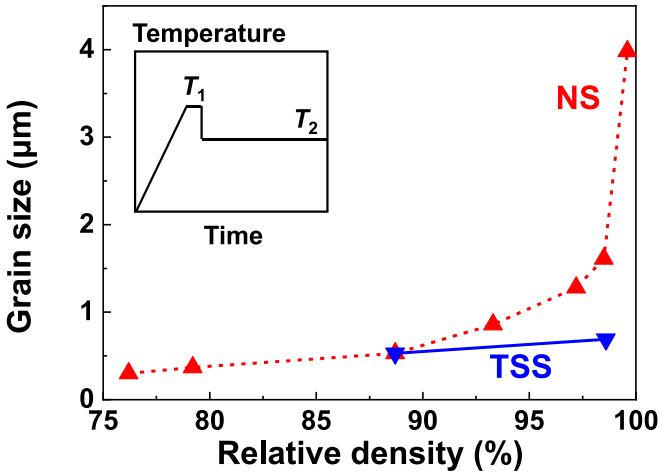

Fig. 2. Grain size-density trajectories in normal sintering and two-step sintering. Inset: Schematic heating profile for two-step sintering.

Furthermore, by plotting the grain size and density of TSS-1 in Fig. 2, it is clear that the trajectory is linear thus accelerated final-stage grain growth is suppressed. This is essential for two-step sintering widely practiced in ceramics community and has now been successfully applied to refractory metals for the first time. (We realized unlike "perfect" two-step sintering, completely frozen grain growth in second-step sintering has not yet been achieved.)

3.2. Microstructures

In addition to the finer grain size, two-step sintering is also able to homogenize the grain microstructure. This is most vividly shown by lower-magnification SEM figures of fracture surfaces in Fig. 4: Unlike normally sintered sample (NS-6; Fig. 4a) suffering from a heterogeneous microstructure with local large-grain regions, two-step sintered sample (TSS-2; Fig. 4b) shows extraordinary uniformity over an large area. The latter is most impressive considering the fact that any mechanically weak microstructural features in W—being brittle at room temperature—would be magnified in fracture. To quantify this effect, EBSD characterizations (Fig. 5) were conducted for samples NS-6 and TSS-2 and their grain size distributions normalized by average grain size G_{avg} were calculated in Fig. 6. While both samples have unimodal grain size distribution, TSS-2 has much smaller standard deviation of normalized grain size (σ = 0.30) than NS-6 (σ = 1.00), and hence is more uniform. (Note σ is a non-dimensional parameter.) Meanwhile, we confirm the average grain sizes obtained from EBSD are similar to the corresponding ones calculated from SEM in Table 1 (G_{avg}=1.65 μm in Fig. 6a vs. 1.60 μm in Table 1 for NS-6; 0.76 μm in Fig. 6b vs. 0.75 μm in Table 1 for TSS-2).

We further investigated the grain orientations from EBSD data. At a first glance of Fig. 5, grain orientations for both samples look random. This is supported by pole figures in Fig. 7: even though sample NS-6 shows higher pole density level (0.20–3.17 mud; "mud" is abbreviated for multiples of a uniform density) than sample TSS-2 (0.51–1.78 mud), neither sample show any obvious texture. Interestingly, the distributions of grain boundary misorientation angles are similar for both samples (Fig. 8) and they all agree well with Mackenzie's distribution [32] for randomly oriented cubic grains (dash line in Fig. 8). The above observations together with the well-maintained equiaxial grain shapes in all the samples suggest relatively isotropic and uniform grain boundary properties for different grain boundaries (in terms of grain boundary energy, mobility, etc.; indeed, W has one of the most isotropic elastic constants among all the metals). Therefore, we expect normal parabolic grain growth takes place in pressurelessly sintered dense sample, as will be shown in the following.

3.3. Grain growth kinetics

To gain more understandings of the microstructural evolution in pure W, we next performed isothermal grain growth experiments. Sintered samples (NS-5 with 97.2% relative density and TSS-1 with 98.0% relative density) were used to minimize the dragging effect of residual porosity on grain boundary migration. Consistent with the literature, apparently parabolic grain growth was confirmed at temperatures from 1300 °C to 1500 °C with 50 °C interval (Fig. 9a), where G_{avg}^2 scales linearly vs. annealing time t. Here, the standard deviation of average grain sizes from three individual measurements (each over 100 grains) was identified as the error bar for each sample, which was then used to calculate the error bars of grain growth data in Fig. 6a. This allows us to use Hillert's normal (parabolic) grain growth model [33] to calculate grain boundary mobility M_b from

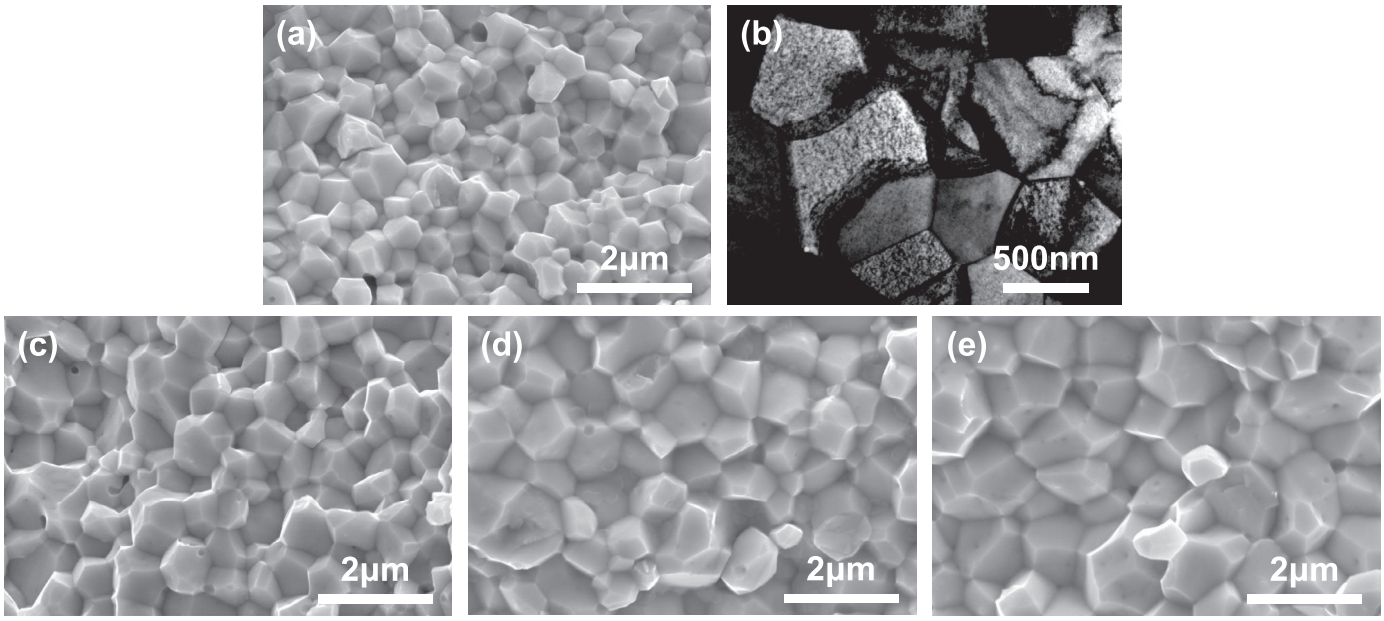

Fig. 3. Fracture surfaces of two-step sintered samples (a) TSS-1 sintered at 1300 °C for 1 h and 1200 °C for 10 h, (c) TSS-2 sintered at 1350 °C for 1 h and 1250 °C for 10 h, (d) TSS-3 sintered at 1400 °C for 1 h and 1300 °C for 10 h, and (e) TSS-4 sintered at 1450 °C for 1 h and 1350 °C for 10 h. Shown in (b) is TEM image of sample (a).

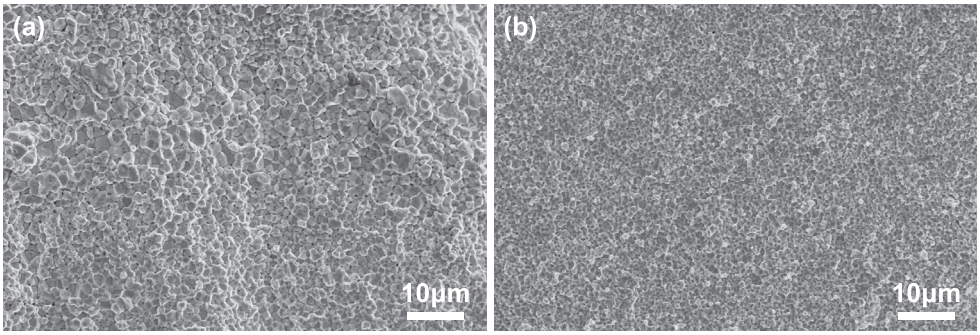

Fig. 4. Lower-magnification images of fracture surfaces of sample (a) NS-6 and (b) TSS-2 showing more homogeneous microstructures of (b).

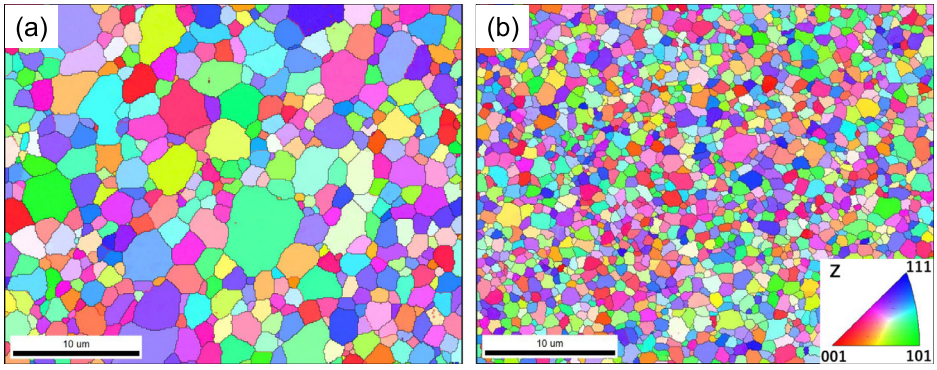

Fig. 5. EBSD mapping for sample (a) NS-6 and (b) TSS-2. Representations for grain orientations shown in inset of (b).

$$G_{avg}^2 - G_0^2 = 2\gamma M_b t \tag{3}$$

where G_0 is initial grain size, γ is grain boundary energy taken as 2.26 J/m^2 [34] for W in the present work. Classically, M_b under normal grain growth was thought thermally activated following Arrhenius-type relationship

$$M_b = M_{b,0} \exp(-Q(T)/k_B T) \tag{4}$$

where $M_{b,0}$ is the pre-exponential factor, k_B is Boltzmann constant, T is absolute temperature in Kelvin, and

$$Q(T) = H(T) - TS(T) \tag{5}$$

is the activation free energy, where $H(T)$ is the activation enthalpy and $S(T)$ is the activation entropy. In a cross-plot between $\ln M_b$ and $1/T$, the slope gives the activation enthalpy

$$-\frac{\partial \ln M_b}{\partial(1/T)} = \frac{\partial\left(Q(T)/k_B T\right)}{\partial(1/T)} = \frac{H(T)}{k_B} \tag{6}$$

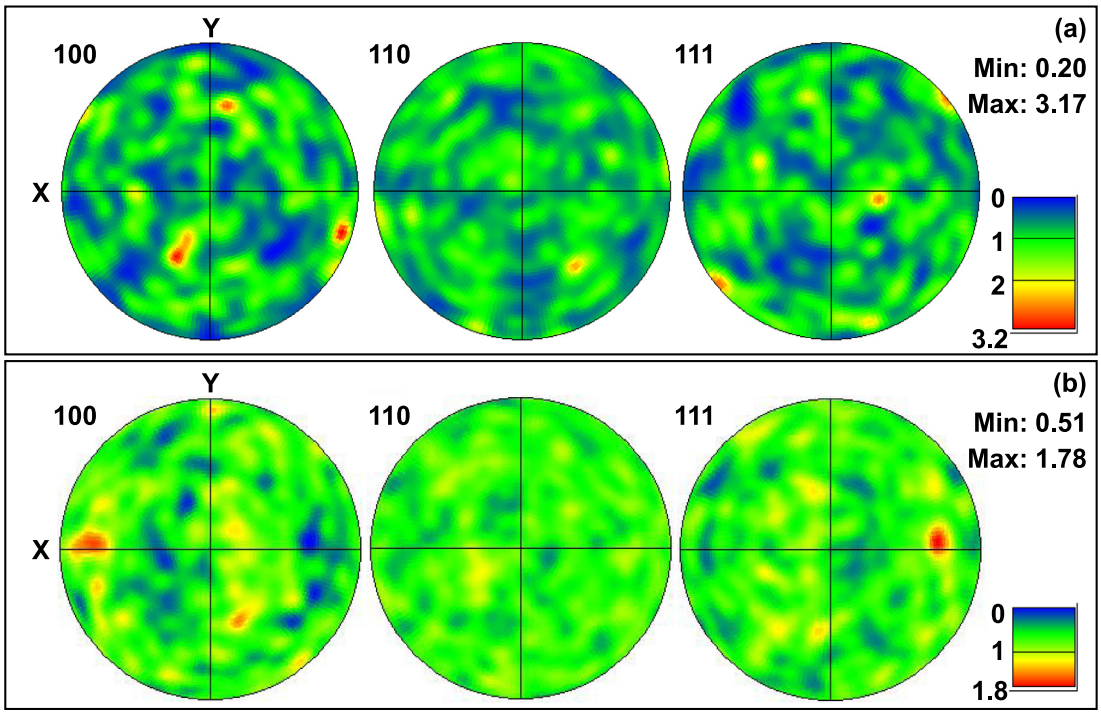

Fig. 6. Normalized grain size distribution of sample (a) NS-6 and (b) TSS-2, calculated from EBSD data. Also listed are G_{avg}, standard deviation σ of normalized grain size G/G_{avg}.

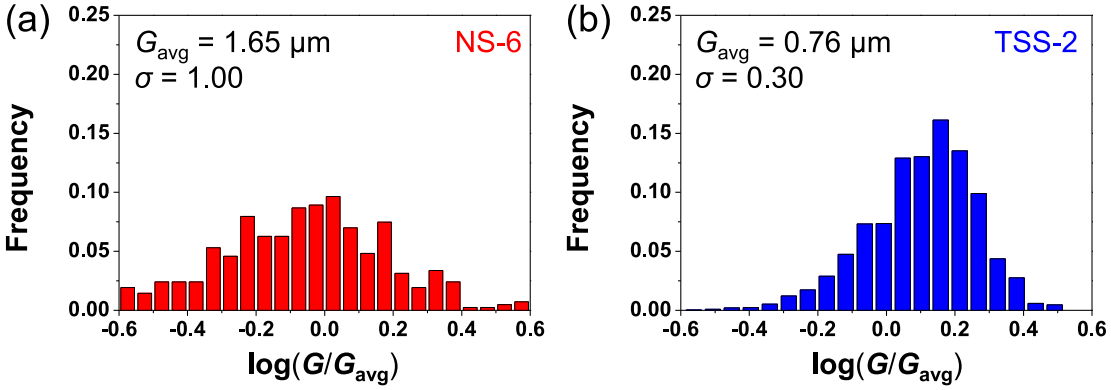

Fig. 7. Pole figures of sample (a) NS-6 and (b) TSS-2 showing more randomly distributed grain orientations of (b).

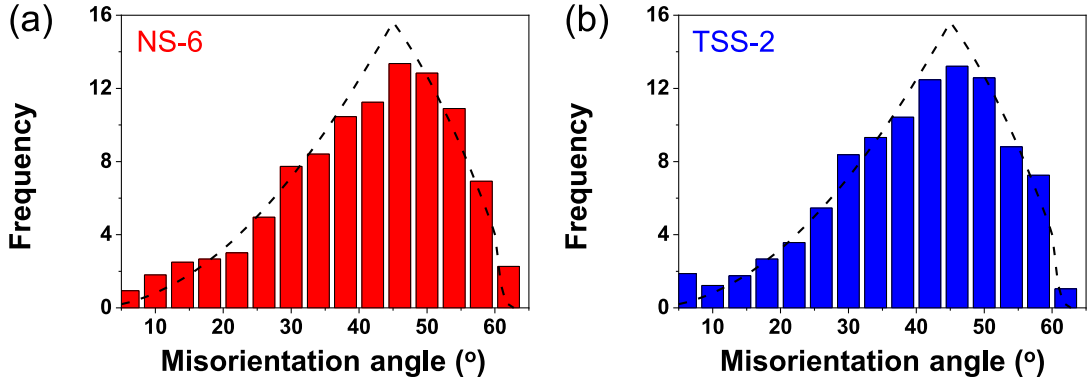

Fig. 8. Distributions of grain boundary misorientation angles of sample (a) NS-6 and (b) TSS-2. Shown by dash line is Mackenzie's distribution for randomly oriented cubic grains.

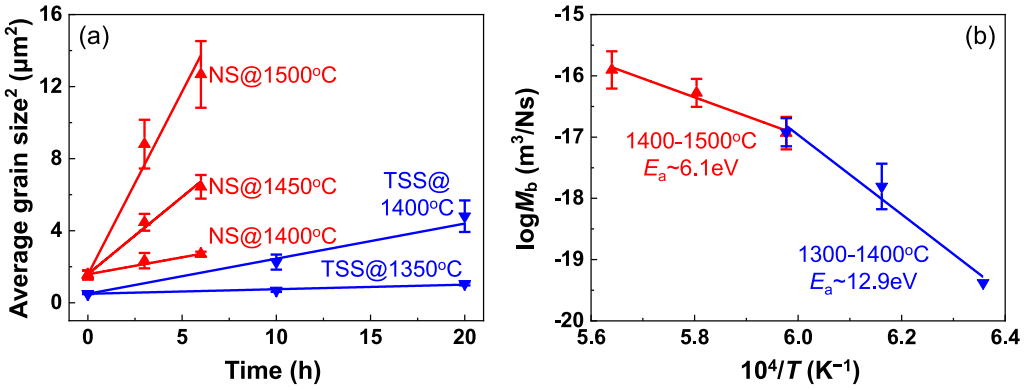

Fig. 9. (a) Grain growth data of normally sintered (denoted as NS in red followed by annealing temperature; using sample NS-5 with 1.24 μm grain size) and two-step sintered dense samples (denoted as TSS in blue followed by annealing temperature; using sample TSS-1 with 0.70 μm grain size) confirming parabolic growth at various temperatures. (b) Arrhenius plot of calculated nominal grain boundary mobility showing stronger dependence at lower temperatures. (For interpretation of the references to color in this figure legend, the reader is referred to the web version of this article.)

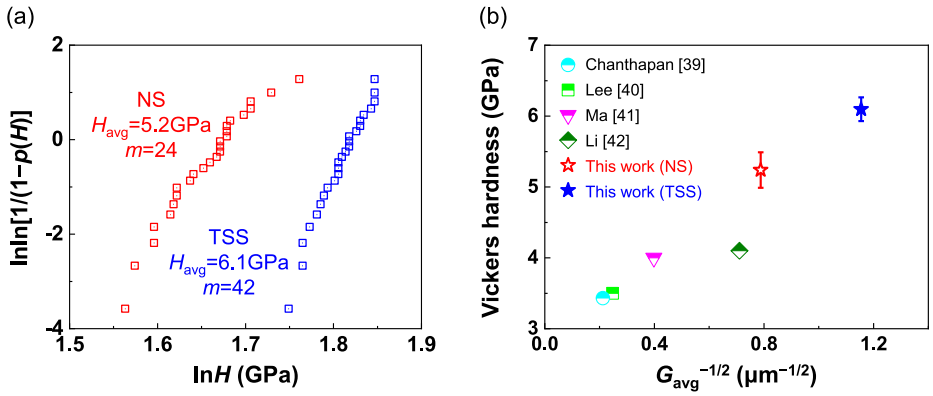

Fig. 10. (a) Weibull distribution of Vickers hardness for two-step sintered (denoted as TSS in blue; using sample TSS-2) and normally sintered samples (denoted as NS in red; using sample NS-6). Average hardness H_{avg} and Weibull modulus m are listed. (b) Comparison of Vickers hardness vs. literature values for dense W [39-42], plotted with inverse square root of average grain size. (For interpretation of the references to color in this figure legend, the reader is referred to the web version of this article.)

according to the Gibbs–Helmholtz equation. If a single mechanism dominates grain boundary migration, then we expect $H(T)$ to vary quite smoothly vs. T.

Yet this is not the case in our dense W as shown by the Arrhenius plot in Fig. 9b, where the curve of M_b is convex even in a narrow temperature range of 200 °C. (Error bars in Fig. 9b were calculated from fitting errors of the slopes in Fig. 9a.) Separate fittings for the high-temperature (1400 °C–1500 °C) and low-temperature (1300 °C–1400 °C) data give an apparent activation enthalpy of 6.1 eV for the former and an unusually large one of 12.9 eV (for W melting at 3695 K) for the latter, respectively. This result is unlikely to come from different samples—sample NS-5 used for 1400 °C–1500 °C and TSS-1 used for 1300 °C–1400 °C—because the two samples have the same M_b at 1400 °C from two sets of individual experiments. Such a large value of 12.9 eV reflects very strong temperature dependence of M_b on temperature, which can be rapidly quenched down especially below 1400 °C. Indeed, these values are much larger than activation enthalpy for grain boundary diffusion in the range of 2.8–4.8 eV obtained from sintering kinetics measurement of W [35-38].

Consistent with the schematic in Fig. 10 of [20] and Fig. 2 of [29], the above provides a numerical justification for two-step sintering, that can suppress grain boundary migration while maintaining active grain boundary diffusion for porosity reduction (sintering) at a lower second-step temperature T_2. The idea is that a lower temperature favors sintering (pore shrinking and disappearing) more than grain coarsening, as reflected in the 2.8–4.8 eV vs. 12.9 eV activation enthalpy. The same data shown in Fig. 9b may also be fitted by a highly nonlinear $H(T)$ within a narrow 200 K range, instead of piecewise linear function, but the basic point is that $H(T)$ increases more rapidly for grain growth than sintering as T decreases. Thus, even though reducing the temperature prolongs the overall heat treatment time to reach below a certain porosity, it comes with the benefits of finer grain sizes. For a fixed total heat-treatment time (which correlate strongly with heat-treatment budget), one may therefore even come up with some multi-step sintering or continuous-cooling sintering protocol to optimize the grain size and properties, beyond two-step sintering which is a simplified protocol.

3.4. Mechanical properties

The finer and more homogeneous microstructure of two-step sintered samples provide better mechanical properties. To illustrate this, three-point bending strength and hardness and reduced Young's

Table 2
Three-point bending strength and hardness and reduced Young's modulus from nanoindentation of normal sintering and two-step sintering samples.

	Bending strength (MPa)	Hardness (GPa)	Reduced Young's modulus (GPa)
NS-6	410	7.0 ± 0.4	374 ± 31
TSS-1	519	/	/
TSS-2	614	7.5 ± 0.4	403 ± 13

modulus from nano-indentation measurements are listed in Table 2, which are all higher for two-step sintered sample (TSS-1 and TSS-2) than normally sintered one (NS-6). For better statistics, Vickers microhardness were measured and analyzed by Weibull statistics. As clearly shown in Fig. 10a, the measured hardness for TSS-2 are much less scattered than NS-6, with Weibull modulus m=42 for the former vs. m=24 for the latter. So the mechanical reliability of two-step sintered W is greatly improved. Lastly, we compared Vickers hardness of our samples with the data of dense tungsten in the literature. As shown in Fig. 10b, our data for both NS-6 and TSS-2 are the highest among all the values; they also follow Hall-Petch relationship well, where Vickers hardness scales linearly with $(G_{avg})^{-1/2}$.

4. Discussions

4.1. Contrasting two-step sintering of tungsten and ceramics

Sintering to "full density" without grain coarsening has been challenging in powder metallurgy and ceramics. The fundamental reason is because densification and grain growth are driven by the similar capillary forces—reduction of surface areas and GB areas, respectively. Their kinetics—atomic diffusion along grain boundary for the former and across grain boundary for the latter—even though not the same, are often difficult to control independently. Nevertheless, there are generally two ways to achieve this. One is to slow down or even halt grain boundary motion by the pinning forces of second-phase particles, and/or solute drag of segregating dopants (which applies to tetragonal zirconia, one of the most celebrated nanoceramics), or pores (in early and intermedium sintering stages, with the best practices up to the beginning of final stage sintering with ~92% theoretical density by suppressing pore-grain boundary breakup). For high-purity (99.9%) W with no artificial doping elements, it is a bit difficult to use the first two pinning mechanisms, and we have seen that the removal of pores tends to drive sharply faster grain growth (Fig. 2, NS) during final-stage sintering. Another way is to provide additional driving force for sintering but not for grain growth. Hot (isostatic) press and high mechanical pressure in SPS work in this way because mechanical pressure only drives pore removal. However, the above methods either change the chemistry or are difficult/expensive to scale up from laboratory to industrial applications.

Two-step sintering works in another way. It postulates that lower temperatures favor sintering compared to grain growth when pore network becomes thermodynamically unstable with $>$ 70%–80% theoretical density. Such a mobility transition has previously been proved in cubic yttria stabilized zirconia [29], and now is also confirmed in pure W. Although further interpretation of such a mobility transition remains to be done, it is clear that the second-step sintering below the transition temperature (seen in Fig. 9b of present work and Fig. 5 of [29]) provides a kinetic origin of successfully two-step sintering of nano-grain samples. This grain boundary mobility transition is expected to be quite general—the successes of two-step sintering in many systems with distinct bonding, chemistry, and crystal structures are a testament to the efficacy.

We noted that even though two-step sintering is successfully practiced to decrease the grain size of full-density W down to submicron, there is still some grain coarsening during second-step sintering. This is in contrast with some optimized ceramic systems where grain growth can be completely suppressed during the second step. We further noted there is also substantial grain growth during first-step sintering, bringing initial particle size of 50 nm for the starting powders to ~500 nm at ~89% theoretical density. These observations suggest the temperatures for both first- and second-step sintering should be further lowered. However, from our experimental experiences, lowering such temperatures cannot lead to full sintering density, even with prolonged holding time. We believe this is due to non-ideal packing of powder compacts, which is critical to the sinterability and density, microstructure, and properties of sintered products. Development of better powders and application of better compacting techniques should be able to solve this problem and provide finer-grain and eventually nanocrystalline samples.

4.2. Grain boundary mobility transition

It is interesting and surprising to find an unusually large activation enthalpy of ~13 eV (for W with a melting temperature T_m of 3695 K) for grain boundary mobility below its transition temperature at 1400 °C (1673 K, ~0.45T_m), which suggests mixed mechanisms involving multiple physical processes. We believe this abnormally large activation enthalpy and mobility transition are less likely to be due to grain boundary phase transitions involving chemical segregations, because we used high-purity (99.9%) W with no artificial doping elements; W is neither as sensitive to impurities as alumina, nor as sensitive to stoichiometry change as perovskites (there is no stoichiometry for W so to speak); and our samples show normal parabolic grain growth, uniform isotropic microstructures and randomly oriented grains without any texture. It is also interesting to note that (i) an unusually large activation enthalpy of 3.2 eV was found for the effective triple junction mobility in aluminum tri-crystals (aluminum has a melting temperature of 933 K), which exceeds twice the activation enthalpy of 2-grain boundary and controls grain boundary motion at lower temperatures [43]; and (ii) atomistic simulations of grain boundary mobility in polycrystals (with grain junctions) and bicrystals (where there is no grain junctions) always find much lower mobility in polycrystals than that in bicrystals [44]. So grain junctions or other multi-grain constraints (between 3, 4, or more adjacent neighboring grains) seem to be relevant and the presence of grain junctions correlates with suppressed grain boundary mobility.

Naively if one disregards the activation entropy (assume $S(T)$=0 in Eq. (5)) contribution, for a 12.9 eV process to compete with a 6.1 eV process at 1400 °C, the former must have a huge advantage in the pre-exponential factor $M_{b,0}$ in Eq. (4), being ~10^{21} larger than that of the latter. Such a large contrast in the pre-exponential factor is difficult to fathom physically, as even the volumetric contributions to the pre-factor (say a 3-dimensional bulk process vs. 2-dimensional boundary process) cannot be this big (0.3 g of W has only ~10^{21} atoms). The involvement of activation entropy $S(T)$ in Eq. (5) seems necessary, so the cooperative motion of many atoms and/or multiple physical processes are likely to be involved. Recently, there have been strong evidence showing large stress generation during grain growth [44] as well as back stress generation associated with diffusive processes in general [45,46]. It is possible that low-temperature grain boundary motion is controlled by stress general/relaxation, especially at grain junctions where stress concentrates [47]; it involves many atoms due to long-range elasticity, thus has a large contribution to the pre-exponential term. In this sense, what we found here may be similar to a glass transition, which is also controlled by stress relaxation and gives a large apparent activation enthalpy near the glass transition temperature. Lastly, one should note that the residual porosity (including their spatial distributions at grain faces, triple lines and four grain junctions) in our samples for grain growth studies could also influence the apparent grain boundary mobility. So more definite measurements in fully dense samples would be worthwhile to explore in future experiments. On the theoretical side, determining the relative importance of pores, grain boundaries, and triple/quadruple junctions by atomistic and mesoscale simulations would be interesting.

5. Conclusion

(1) Pressureless two-step sintering has been successfully applied to pure W. It can provide fine grain sizes (~700 nm) and uniform

microstructures with narrow size distributions for dense W (~99% theoretical density), without any observable texture, abnormal grain growth, second-phase impurities or grain-boundary liquids (after cooling down).

(2) A transition of grain boundary mobility was observed at 1400 °C for as-sintered dense samples. The apparent activation enthalpy dramatically increases from ~6.1 eV between 1400 °C and 1500 °C to unusually high value of ~12.9 eV between 1300 °C and 1400 °C, suggesting rapidly diminishing grain growth kinetics below 1400 °C.

(3) This highly nonlinear behavior in the activation parameters of grain growth kinetics in a randomly oriented polycrystalline sample vs. temperature (which was also observed in yttria stabilized zirconia in [29]) is still not clear at this stage, which is worthwhile for further theoretical studies. We speculate it to involve activation entropy and maybe collective/nonlocal behavior of multiple grains (or voids).

(4) Mechanical properties of two-step sintered samples are greatly improved, due to finer and much more uniform microstructures.

(5) We expect pressureless two-step sintering to be applicable to other refractory metals and their alloys. This protocol may be further generalized to multi-step or continuous-cooling sintering design using machine learning. Further experiments are in progress and shall be reported in forthcoming papers.

Acknowledgment

X. L., L. Z., M. Q., X. Q. acknowledge the financial support by National Key R&D Program of China (2017YFB0305600), Natural Science Foundation of China (51574029) and 111 Project (No. B170003). J. L. acknowledges support by Eni and NSF CMMI-1922206.

Declaration of competing interest

The authors declare that they have no known competing financial interests or personal relationships that could have appeared to influence the work reported in this paper.

References

[1] W.F. Smith, Structure and Properties of Engineering Alloys, 2nd ed., McGraw Hill, New York, 1993.
[2] J.L. Johnson, Sintering of refractory metals, in: Z.Z. Fang (Ed.), Sintering of Advanced Materials-Fundamentals and Processes, Woodhead Publishing, Cambridge, UK, 2010, pp. 356–388.
[3] G. Prabhu, A. Chakraborty, B. Sarma, Microwave sintering of tungsten, Int. J. Refract. Met. Hard Mater. 27 (2009) 545–548.
[4] P. Liu, F. Peng, F. Liu, H. Wang, C. Xu, Q. Wang, et al. High-pressure preparation of bulk tungsten material with near-full densification and high fracture toughness, Int. J. Refract. Met. Hard Mater. 42 (2014) 47–50.
[5] M.A. Monge, M.A. Auger, T. Leguey, Y. Ortega, L. Bolzoni, E. Gordo, et al. Characterization of novel W alloys produced by HIP, J. Nucl. Mater. 386–388 (2009) 613–617.
[6] Y. Kim, K. Ho, E. Kim, D. Cheong, S. Hyung, Fabrication of high temperature oxides dispersion strengthened tungsten composites by spark plasma sintering process, Int. J. Refract. Met. Hard Mater. 27 (2009) 842–846.
[7] L. Huang, L. Jiang, T.D. Topping, C. Dai, X. Wang, R. Carpenter, et al. In situ oxide dispersion strengthened tungsten alloys with high compressive strength and high strain-to-failure, Acta Mater. 122 (2017) 19–31.
[8] H.W. Hayden, J.H. Brophy, The activated sintering of tungsten with group VIII elements, J. Electrochem. Soc. 110 (1963) 805–810.
[9] N.M. Hwang, Y.J. Park, D. Kim, D.Y. Yoon, Activated sintering of nickel doped tungsten: approach by grain boundary structural transition, Scr. Mater. 42 (2000) 421–425.
[10] K.S. Hwang, H.S. Huang, Identification of the segregation layer and its effects on the activated sintering and ductility of Ni-doped molybdenum, Acta Mater. 51 (2003) 3915–3926.
[11] V.K. Gupta, D. Yoon, H.M. Meyer, J. Luo, Thin intergranular films and solid-state activated sintering in nickel-doped tungsten, Acta Mater. 55 (2007) 3131–3142.
[12] J. Luo, V.K. Gupta, D.H. Yoon, Segregation-induced grain boundary premelting in nickel-doped tungsten, Appl. Phys. Lett. 87 (2005) 231902.
[13] H. Wang, Z.Z. Fang, K.S. Hwang, H. Zhang, D. Siddle, Sinter-ability of nanocrystalline tungsten powder, Int. J. Refract. Met. Hard Mater. 28 (2010) 312–316.
[14] X. Wang, Z.Z. Fang, M. Koopman, The relationship between the green density and as-sintered density of nano-tungsten compacts, Int. J. Refract. Met. Hard Mater. 53 (2015) 134–138.
[15] C. Ren, Z.Z. Fang, H. Zhang, M. Koopman, The study on low temperature sintering of nano-tungsten powders, Int. J. Refract. Met. Hard Mater. 61 (2016) 273–278.
[16] Z.Z. Fang, H. Wang, V. Kumar, Coarsening, densification, and grain growth during sintering of nano-sized powders—a perspective, Int. J. Refract. Met. Hard Mater. 62 (2017) 110–117.
[17] C. Ren, Z.Z. Fang, M. Koopman, H. Zhang, The effects of molybdenum additions on the sintering and mechanical behavior of ultrafine-grained tungsten, JOM 70 (2018) 2567–2573.
[18] C. Ren, Z.Z. Fang, L. Xu, J.P. Ligda, J.D. Paramore, B.G. Butler, An investigation of the microstructure and ductility of annealed cold-rolled tungsten, Acta Mater. 162 (2019) 202–213.
[19] I.W. Chen, X.H. Wang, Sintering dense nanocrystalline ceramics without final-stage grain growth, Nature 404 (2000) 168–171.
[20] X.H. Wang, P.L. Chen, I.W. Chen, Two-step sintering of ceramics with constant grain-size, I. Y_2O_3, J. Am. Ceram. Soc. 89 (2006) 431–437.
[21] X.H. Wang, X.Y. Deng, H.L. Bai, H. Zhou, W.G. Qu, L.T. Li, et al. Two-step sintering of ceramics with constant grain-size, II: $BaTiO_3$ and Ni-Cu-Zn ferrite, J. Am. Ceram. Soc. 89 (2006) 438–443.
[22] R. Guo, W. Cao, X. Mao, J. Li, Selective corrosion preparation and sintering of disperse α;-Al_2O_3 nanoparticles, J. Am. Ceram. Soc. 99 (2016) 3556–3560.
[23] H. Yang, L. Li, W. Cao, Y. Liu, M. Mukhtar, L. Zhao, et al. Sintering kinetics and microstructure evolution in α;-Al2O3 nanocrystalline ceramics: insensitive to Fe impurity, J. Eur. Ceram. Soc., 10.1016/j.jeurceramsoc.2019.11.079.
[24] M. Mazaheri, A. Simchi, F. Golestani-Fard, Densification and grain growth of nanocrystalline 3Y-TZP during two-step sintering, J. Eur. Ceram. Soc. 28 (2008) 2933–2939.
[25] M. Mazaheri, A.M. Zahedi, S.K. Sadrnezhaad, Two-step sintering of nanocrystalline ZnO compacts: effect of temperature on densification and grain growth, J. Am. Ceram. Soc. 91 (2008) 56–63.
[26] M. Mazaheri, Z. Razavi Hesabi, S.K. Sadrnezhaad, Two-step sintering of titania nanoceramics assisted by anatase-to-rutile phase transformation, Scr. Mater. 59 (2008) 139–142.
[27] Q. Zhao, H. Gong, X. Wang, I.W. Chen, L. Li, Superior reliability via two-step sintering: barium titanate ceramics, J. Am. Ceram. Soc. 99 (2016) 191–197.
[28] J.L. Johnson, Progress in processing nanoscale refractory and hardmetal powders, in: Proceeding of the International Conference on W, Refractory & Hardmaterials VII, 2008, pp. 57–71.
[29] Y. Dong, I.W. Chen, Mobility transition at grain boundaries in two-step sintered 8 mol% yttria-stabilized zirconia, J. Am. Ceram. Soc. 101 (2018) 1857–1869.
[30] M. Qin, Z. Chen, P. Chen, S. Zhao, R. Li, J. Ma, et al. Fabrication of tungsten nanopowder by combustion-based method, Int. J. Refract. Met. Hard Mater. 68 (2017) 145–150.
[31] B. Bergman, On the estimation of the Weibull modulus, J. Mater. Sci. Lett. 3 (1984) 689–692.
[32] J.K. Mackenzir, Second paper on statistics associated with the random disorientation of cubes, Biometrika 45 (1958) 229–240.
[33] M. Hillertt, On the theory of normal and abnormal grain growth, Acta Mater. 13 (1965) 227–238.
[34] D. Scheiber, R. Pippan, P. Puschnig, L. Romaner, *Ab initio* calculations of grain boundaries in bcc metals ab initio calculations of grain boundaries in bcc metals, Model. Simul. Mater. Sci. Eng. 24 (2016) 035013.
[35] H. Materials, P. Schade, Sintering behavior of spherical mono-sized tungsten powder, Int. J. Refract. Met. Hard Mater. 74 (2018) 14–19.
[36] R.M. German, Z.A. Munir, Enhanced low-temperature sintering of tungsten, Metall. Trans. A 7 (1976) 1873–1877.
[37] Z. Gao, G. Viola, B.E.N. Milsom, I. Whitaker, H. Yan, M.J. Reece, Kinetics of densification and grain growth of pure tungsten during spark plasma sintering, Metall. Mater. Trans. B 43 (2012) 1608–1614.
[38] S. Deng, T. Yuan, R. Li, F. Zeng, G. Liu, X. Zhou, Spark plasma sintering of pure tungsten powder: densification kinetics and grain growth, Powder Technol. 310 (2017) 264–271.
[39] S. Chanthapan, A. Kulkarni, J. Singh, C. Haines, D. Kapoor, Sintering of tungsten powder with and without tungsten carbide additive by field assisted sintering technology, Int. J. Refract. Met. Hard Mater. 31 (2012) 114–120.
[40] G. Lee, J. Mckittrick, E. Ivanov, E.A. Olevsky, Densification mechanism and mechanical properties of tungsten powder consolidated by spark plasma sintering, Int. J. Refract. Met. Hard Mater. 61 (2016) 22–29.
[41] J. Ma, J. Zhang, W. Liu, Z. Shen, Suppressing pore-boundary separation during spark plasma sintering of tungsten, J. Nucl. Mater. 438 (2013) 199–203.
[42] B. Li, Z. Sun, G. Hou, F. Ding, P. Hu, F. Yuan, The sintering behavior of quasi-spherical tungsten nanopowders, Int. J. Refract. Met. Hard Mater. 56 (2016) 44–50.
[43] S.G. Protasova, G. Gottstein, D.A. Molodov, V.G. Sursaeva, L.S. Shvindlerman, Triple junction motion in aluminum tricrystals, Acta Mater. 49 (2001) 2519–2525.
[44] J. Han, S.L. Thomas, D.J. Srolovitz, Grain-boundary kinetics: a unified approach, Prog. Mater. Sci. 98 (2018) 386–476.
[45] I.A. Blech, Diffusional back flows during electromigration, Acta Mater. 46 (1998) 3717–3723.
[46] D.G. Xie, Z.Y. Nie, S. Shinzato, Y.Q. Yang, F.X. Liu, S. Ogata, J. Li, E. Ma, Z.W. Shan, Controlled growth of single-crystalline metal nanowires via thermomigration across a nanoscale junction, Nat. Commun. 10 (2019) 4478.
[47] K. McReynolds, K. Wu, P. Voorhees, Grain growth and grain translation in crystals, Acta Mater. 120 (2016) 264–272.